Evaluation of Several Explanations of the Strong X-Ray Polarization of the Black Hole X-Ray Binary 4U 1630-47

Henric Krawczynski[1] , Yajie Yuan[2] , Alexander Y. Chen[2] , Kun Hu[1] , Nicole Rodriguez Cavero[1] , Sohee Chun[1] ,
Ephraim Gau[1] , James F. Steiner[3] , and Michal Dovčiak[4]

[1] Physics Department, McDonnell Center for the Space Sciences, and Center for Quantum Leaps, Washington University in St. Louis, St. Louis, MO 63130, USA;
krawcz@wustl.edu

[2] Physics Department and McDonnell Center for the Space Sciences, Washington University in St. Louis, St. Louis, MO 63130, USA; yajiey@wustl.edu,
cyuran@wustl.edu

[3] Harvard-Smithsonian Center for Astrophysics, 60 Garden Street, Cambridge, MA 02138, USA

[4] Astronomical Institute of the Czech Academy of Sciences, Boční II 1401/1, 14100 Praha 4, Czech Republic

Abstract

The Imaging X-ray Polarimetry Explorer observations of the X-ray binary 4U 1630–47 in the high soft state revealed high linear polarization degrees (PDs) rising from 6% at 2 keV to 10% at 8 keV. We discuss in this Letter three different mechanisms that impact the polarization of the observed X-rays: the reflection of gravitationally lensed emission by the accretion disk, reprocessing of the emission in outflowing plasma, and electron and ion anisotropies in the accretion disk atmosphere. We conducted detailed ray-tracing studies to evaluate the impact of the reflection of strongly gravitationally lensed emission on the PDs. Although the reflected emission can produce high PDs in the high-energy tail of the thermal emission component, we do not find models that describe the PDs and are consistent with independent estimates of the source distance. We discuss the energetics of another proposed mechanism: the emission or scattering of the X-rays in mildly relativistically moving plasma outflows. We argue that these models are disfavored as they require large mechanical luminosities on the order of, or even exceeding, the Eddington luminosity. We investigated the impact of electron and ion anisotropies but find that their impact on the observed PDs are likely negligible. We conclude with a discussion of all three effects and avenues for future research.

1. Introduction

The Imaging X-ray Polarimetry Explorer (IXPE; M. C. Weisskopf et al. 2022) launched on 2021 December 9 measured or constrained the polarization of the X-rays from several black hole X-ray binaries (BHXRBs). In the thermally dominated soft state, IXPE observations allow us to test the standard geometrically thin, optically thick accretion disk model, and—if verified—to constrain the source inclination (L.-X. Li et al. 2009) and black hole spin (J. D. Schnittman & J. H. Krolik 2009). In the hard state (HS), the IXPE observations constrain the geometry, location, and physical properties of the hard-X-ray-emitting corona and the inclination of the accretion flow (H. Krawczynski et al. 2022). To date, IXPE has observed six X-ray BHXRBs with data in the public domain (N. Rodriguez Cavero & IXPE Collaboration 2024). Three black holes were observed in more than one emission state: Cyg X-1 in the hard state (HS) and in the high soft state (HSS; H. Krawczynski et al. 2022; M. Dovciak et al. 2023; A. Jana & H.-K. Chang 2024), 4U 1630−47 in the HSS and in the steep power-law (SPL) state (N. Rodriguez Cavero et al. 2023; A. Ratheesh et al. 2024), and Swift J1727.8–1613 in the HS, an intermediate disk-dominated state, and in a dim HS (A. Veledina et al. 2023; A. Ingram et al. 2024; J. Podgorný et al. 2024). The black holes LMC X-1 (J. Podgorny et al. 2023), LMC X-3

(J. Svoboda et al. 2024), and 4U 1957+115 (L. Marra et al. 2024) were observed in the soft state. The observations of the black hole candidate Cyg X-3 in the HS led to the reclassification of the source as an ultraluminous X-ray source, which emits strongly polarized X-rays owing to the reflection of X-rays off funnel walls (A. Veledina et al. 2024). The source has most recently also been observed in the soft state (A. Veledina et al. 2024; N. Rodriguez Cavero et al. 2024, in preparation).

In this Letter, we focus on 4U 1630–47, a low-mass X-ray binary (LMXB) with recurrent outbursts every 2–3 yr (E. Kuulkers et al. 1998; F. Capitanio et al. 2015). The IXPE observations of the HSS are particularly interesting as they probe the polarization of the emission from the optically thick geometrically thin accretion disk and thus allow us to test the classical thin disk theory (N. I. Shakura & R. A. Sunyaev 1973). The IXPE observations revealed PDs increasing from ∼6% at 2 keV to ∼10% at 8 keV in the HSS (A. Ratheesh et al. 2024) and increasing from ∼5% at 2 keV to ∼8% at 8 keV in the SPL state. For both observations, the polarization angles (PAs) did not exhibit statistically significant variations with energy or time.

The PDs measured in the HSS are high compared to theoretical expectations (J. D. Schnittman & J. H. Krolik 2009; L.-X. Li et al. 2009; W. Zhang et al. 2019; R. Taverna et al. 2020; H. Krawczynski & B. Beheshtipour 2022; A. Ratheesh et al. 2024). According to Chandrasekhar's classical treatment, the emission from an electron scattering atmosphere creates PDs of between 0% (0° inclination) and 11.71% (90° inclination) (S. Chandrasekhar 1960). The inclination of

4U 1630–47 is estimated to be ∼65° (E. Kuulkers et al. 1998; J. A. Tomsick et al. 1998) for which Chandrasekhar's PD equals 2.8%. Furthermore, strong gravitational lensing tends to reduce the observed PDs as the polarization of photons that traveled through the curved spacetime close to the black hole and scattered off the accretion disk partially cancels the polarization of the photons emitted farther away from the black hole (A. Ratheesh et al. 2024). The latter authors manage to explain the IXPE results with a model combining three effects that increase the PD of the emission: a low black hole spin (reducing the effects from strong lensing), the emission of highly polarized X-rays by a partially ionized plasma, and the emitting plasma streaming with 50% of the speed of light away from the accretion disk. The latter effect increases the observed PDs as X-rays emitted at higher local inclinations reach the observer at the binary inclination owing to relativistic aberration. The same authors discuss two other scenarios but find that they cannot explain the IXPE results: slim disks generate higher PDs than thin disks (A. T. West & H. Krawczynski 2023) but still not as high as the observed ones; the reflection of the X-rays off a wind cannot explain the rise of the PDs with energy (A. Veledina et al. 2024). Detailed modeling of the emission from systems with winds confirm these results and show that the wind reflection reduces rather than increases the PD of the emission (R. Tomaru et al. 2024).

In this Letter, we discuss three mechanisms that may contribute to the polarization of the X-rays from 4U 1630–47. Section 2 presents the results from fitting the 4U 1630–47 data with the general relativistic ray-tracing model `kerrClight`. Although the reflection of strongly gravitationally lensed disk emission increases the observable PDs, we do not find model parameters that fit the high PDs of 4U 1630–47 and are consistent with independent constraints on the source distance. We discuss alternative models involving outflowing emitting plasmas in Section 3. We find that these models require plasma outflows with high mechanical luminosities. Section 4 discusses the possible impact of electron and/or ion anisotropies on the polarization of the disk emission. Although order unity anisotropies can lead to highly polarized bremsstrahlung and Compton scattered emission, we find that this effect is unlikely to play a role in the HSS of BHXRBs as Coulomb collisions limit particle anisotropies to very small levels.[5] We conclude with a discussion of our findings in Section 5.

The polarized radiation transport code described in the Appendix has been published as a Zenodo archive (H. Krawczynski & B. Beheshtipour 2024).

2. Fitting of the IXPE, NICER, and NuSTAR HSS Data with `kerrClight`

In this section, we analyze the IXPE, NICER, and NuSTAR observations of 4U 1630–47 in HSS using the data sets described in Appendix A of A. Ratheesh et al. (2024). The IXPE observations were acquired between 2022 August 23 and 2022 September 2 and were reduced with the standard methods (L. Baldini et al. 2022); 27 ks of NICER observations were acquired between 2022 August 22 and 2022 September 1 and were reduced with the `NICERDAS` software (v. 09) of the HEASOFT web package (High Energy Astrophysics Science Archive Research Center (HEASARC) 2014); lastly, a total of

---

∼70 ks of NuSTAR observations were acquired between 2022 August 25 and 29 and were reduced with the `NuSTARDAS` software package (v. 2.1.2), also part of the HEASOFT suite. We use the IXPE data from 2 to 8 keV, the NICER data from 2 to 8 keV, and the NuSTAR data from 3 to 40 keV.

We analyze the data with the `kerrClight` X-ray fitting model. The model is a simplified version of the more general `kerrC` fitting model (H. Krawczynski & B. Beheshtipour 2022), which assumes a geometrically thin, optically thick Novikov–Thorne accretion disk interacting with 3D coronas of hot plasma of different shapes, i.e., wedge-shaped coronas sandwiching the accretion disk, and cone-shaped coronas centered on the black hole spin axis. The accretion disk extends from the radial distance of the innermost circular orbit r_{ISCO} to $100\,r_{\mathrm{g}}$ ($r_{\mathrm{g}} \equiv GM/c^2$, with G being the gravitational constant, M being the black hole mass, and c being the speed of light), and the code assumes that the angular momentum vectors of the black hole and the accretion disk are aligned. The code is based on ray-tracing photons from the disk to the observer accounting for scatterings off the disk and in the corona. Assuming a high ionization of the photospheric and coronal plasma, `kerrClight` implements the scattering off the disk based on Chandrasekhar's prescription for the reflection of polarized beams off an indefinitely deep scattering atmosphere (S. Chandrasekhar 1960). In contrast to `kerrC`, `kerrClight` does not account for the reprocessing of X-rays in a partially ionized photosphere (J. García & T. R. Kallman 2010; J. García et al. 2013). Indeed, detailed modeling of the 4U 1630–47 data largely validates this assumption (A. Ratheesh et al. 2024, Appendix B). We only consider sandwich coronas here, led by the constraints on the shape of the corona of Cyg X-1 in the HS (H. Krawczynski et al. 2022). The `kerrClight` model parameters describing the black hole system and the corona are the black hole mass M, the black hole spin parameter a ($-1 \leqslant a \leqslant 1$), inclination (angle of the observer relative to the black hole spin axis) i, black hole distance D, mass accretion rate $\dot{M}$, the radial extent of the corona r_{C} (the corona extends from r_{ISCO} to r_{C}), the corona half-opening angle θ_{C}, the coronal electron temperature T_{C}, the corona optical depth τ_{C} (measured vertically above the disk to the upper and lower edge of the corona), the albedo (i.e., the reflectivity of the disk, relative to 100% reflection), as well as the angle χ between the black hole axis and the celestial north pole (positive for an anticlockwise rotation). Note that the reflecting disk reaches down through the corona to $r = r_{\mathrm{ISCO}}$. For low optical depths, the 100% reflectivity of the disk enhances the intensity of the coronal emission substantially as photons scattering in the corona backwards toward the disk experience much larger energy gains than photons scattering forward away from the disk and toward the observer. Owing to the steeply falling energy spectrum of the coronal emission, the larger energy gains translate into a substantial flux enhancement.

We fit the Stokes I, Q, and U energy spectra for all three IXPE telescopes, the NICER Stokes I energy spectrum, and the NuSTAR Stokes I energy spectra of the two NuSTAR telescopes of Observations 1 and 2 (NuSTAR IDs 80802313002 and 80802313004). The fits include constant scaling factors to account for the flux variability between the IXPE, NICER, and NuSTAR observations.

Overall, we find that `kerrClight` does not give statistically acceptable fits, and we do not report the χ^2 values here. Even though the fits are not perfect, they are interesting as

they confront the experimental data with the predictions of the standard thin disk accretion disk model.

We show two exemplary `kerrClight` models. The first model (see Figure 1 and Table 1) assumes a fiducial black hole mass of $10 M_\odot$, a distance of 11.5 kpc (E. Kalemci et al. 2018), and an inclination of 70° consistent with the presence of dips but the absence of eclipses in the X-ray light curves of 4U 1630 −47 (E. Kuulkers et al. 1998; J. A. Tomsick et al. 1998). We chose a black hole spin parameter of $a = 0.75$, a corona extending from 1 to 25 r_g, a corona temperature of $T_C = 100$ keV, and a coronal optical depth τ_C of 0.0035 to obtain a good description of the broadband spectral energy distribution (SED) measured with NICER, IXPE, and NuS-TAR. We fit the neutral hydrogen column density n_H, the mass accretion rate $\dot{M}$, and the PA χ of the black hole and accretion disk spin axis. The model predicts PDs of around 1% and can thus not account for the IXPE results between 6% and 10%. The result of the modeled PDs being much lower than the observed ones is valid for a large portion of the parameter space.

We forced `kerrClight` to give a better description of the X-ray polarization results by arbitrarily multiplying the IXPE errors of Stokes I and Stokes Q and U by factors of 10^{-2} (I) and 10^{-6} (Q and U). The preferred fits combine high black hole masses of $\sim 40 M_\odot$ with small system distances of $\leqslant 1$ kpc. Such small distances are inconsistent with the distance constraint $D > (4.63 \pm 0.25)$ kpc from the condition that the source is positioned behind the molecular cloud MC−79 (E. Kalemci et al. 2018). Figure 2 shows one of the best models (see Table 1 for the model parameters), that of combining a black hole mass of $40 M_\odot$ with a small distance of $D = 0.35$ kpc and a high spin of $a = 0.992$. The high black hole mass and small distance lead to a low accretion rate and to a low temperature scale of the multitemperature blackbody disk emission. This makes the disk spectrum relatively soft. The high spin, and thus small inner disk truncation radius, lead to a high fraction of high-energy photons being emitted close to the black hole to return to the accretion disk due to strong gravitational lensing and to reflect off the disk (see also J. D. Schnittman & J. H. Krolik 2009; J. F. Steiner et al. 2024). Owing to the Doppler boosting and deboosting of these photons reflecting off the disk, the reflected energy spectrum is broader than that of the disk emission. Due to the steeply falling energy spectrum, the reflected emission strongly dominates the emitted blackbody spectrum in the IXPE energy range. Figure 2 shows that this model can roughly generate the observed PDs and PAs as a function of energy. Note that the model explains the SED, including the high-energy power-law tail, even though it assumes a disk without a corona (i.e., with a `kerrClight` corona optical depth of $\tau_C = 0$). The high-energy power-law tail results from some photons returning multiple times to the accretion disk owing to strong gravitational lensing and, on average, gaining energy when scattering off the disk. The accretion disk of a rapidly spinning black hole can thus emit a power-law component just like a corona. In the former case, photons experience multiple scatterings owing to the spacetime curvature close to the black hole; in the latter case, they experience multiple scatterings owing to being (temporarily) trapped inside the corona. Note that other models, e.g., `KERRBB` (L.-X. Li et al. 2005), fail to predict such power-law tails as they do not model the net effect of photons
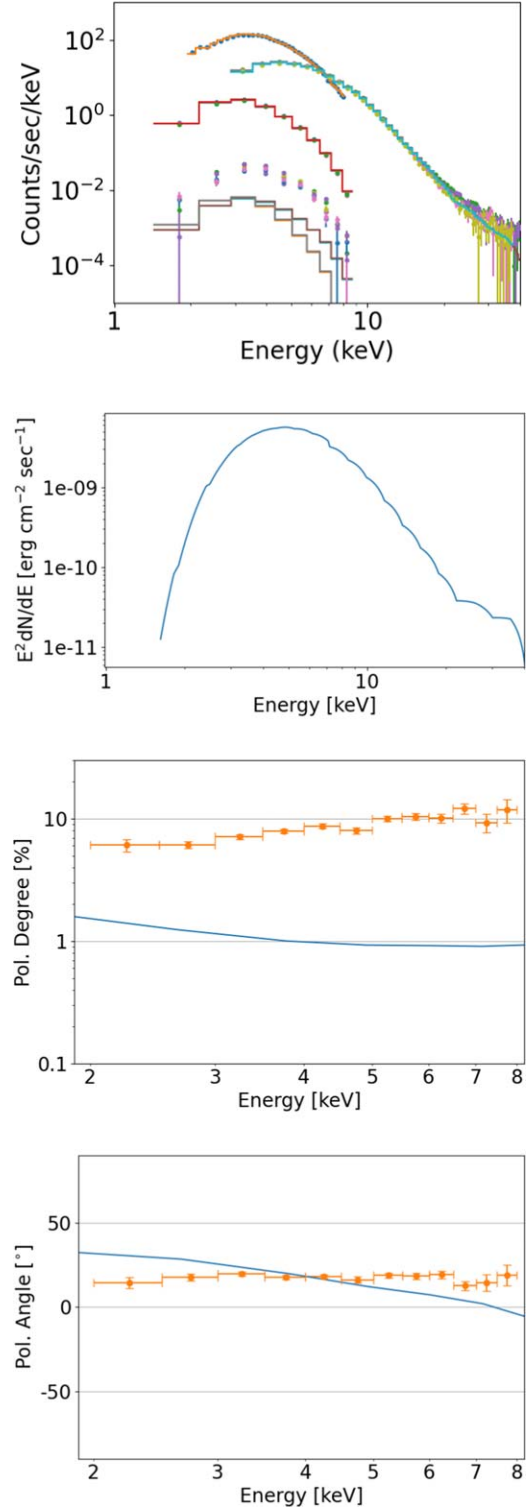

Figure 1. Exemplary `kerrClight` result assuming black hole mass of $10 M_\odot$, a system distance of 11.5 kpc, and a 70° inclination. The panels show the observed and modeled flux and Stokes I, Q, and U energy spectra (top), the model SED (upper center), PD (lower center), and PA (bottom) as a function of energy. In the upper panel, the data points show, from the top to the bottom, the NICER energy spectrum, the energy spectra of the two NuSTAR telescopes for two observations, the energy spectra (Stokes I) of the three IXPE detectors, and Stokes Q and U energy spectra of the three IXPE telescopes (see Table 1 for the fit parameters). In the bottom panel, the PA is measured east from the celestial north with the angle increasing for a counterclockwise rotation looking toward the source. For the model, the black hole spin axis is at a PA of 52°.82.

Table 1
`kerrClight` Parameters of Figures 1 and 2

Parameter	Units	Figure 1	Figure 2
Black hole spin a	...	0.75[c]	0.992[c]
Black hole mass M	$M_\odot$	10[c]	40[c]
Inclination i	deg	70[c]	72.20
Accretion rate $\dot{M}$	10^{18} g s^{-1}	4.14	0.074
Distance D	kpc	11.5[c]	0.35[c]
χ[a]	deg	52.82	-11.83
Corona optical depth τ_C	...	0.0035[c]	0[b,c]
Corona electron temperature T_C	keV	100[c]	...
Corona inner radius r_1	r_{ISCO}	1[c]	...
Corona outer radius r_2	r_{ISCO}	25[c]	...
Corona half-opening angle θ_C	deg	5	...
Albedo	...	1	1
H I column density n_H	10^{21} cm^{-2}	12.96	22.50[c]

Notes.
[a] Angle of disk angular momentum vector projected into the plane of the sky east from the celestial north.
[b] $\tau_C = 0$ means that there is only a thin disk and no corona.
[c] Frozen parameter.

scattering multiple times off the accretion disk and the frequency shifts associated with Doppler boosting the photons' wavevectors into and out of the accretion disk frame for each scattering. As a consequence of the reflected gravitationally lensed emission dominating the X-ray polarization of this model, the electric vector PA is roughly aligned with the black hole spin axis. Note that most simulated photons of the low-luminosity model of Figure 2 have <2 keV energies, and the energy spectra predicted with 20×10^6 photons have noticeable statistical errors.

3. Energetics of Outflowing Plasma Models

A. Ratheesh et al. (2024) invoke an outflowing plasma as an explanation of the high polarization degrees of 4U 1530$-$47. In this section, we discuss the energetics required for such outflows.

Assuming an outflowing photosphere emits via bremsstrahlung, we can set limits on the photospheric ion and electron densities. For electron density n_e and ion density n_i the electron-ion bremsstrahlung volume emissivity is (G. Rybicki & A. Lightman 2008)

$$\epsilon_{ff} \approx 1.7 \times 10^{-27} \sqrt{T} \, n_e \, n_i \text{ erg s}^{-1} \text{ cm}^{-3}. \quad (1)$$

Assuming that the emission comes from a cylinder of inner and outer radii $2\,r_g$ and $10\,r_g$ and height $h_{max} = 10\,r_g$ as well as $n_e = n_i$, we infer electron and ion densities exceeding 2.3×10^{19} cm^{-3} so that the emitted power per area $\epsilon_{ff}\,h_{max}$ equals a diluted blackbody emissivity $I = \sigma_B(T/f)^4 \approx 1.8 \times 10^{23}$ erg s^{-1} cm^{-2} for $k_B\,T = 1.1$ keV and a hardening factor of $f = 1.7$.

We can use these estimates to derive limits on the kinetic luminosity of a plasma moving with $\beta = 0.5$ times the velocity of light:

$$L_{kin} = (\gamma - 1)\mu_e \, n_e \, M_p \, c^2 \, A \, \beta \, c, \quad (2)$$

where $\gamma = (1 - \beta^2)^{-1/2}$ and $\mu_e \approx 1.3$ is the mean molecular weight of the ions per electron in units of the proton mass. For a plasma dense enough to create the observed X-ray luminosity
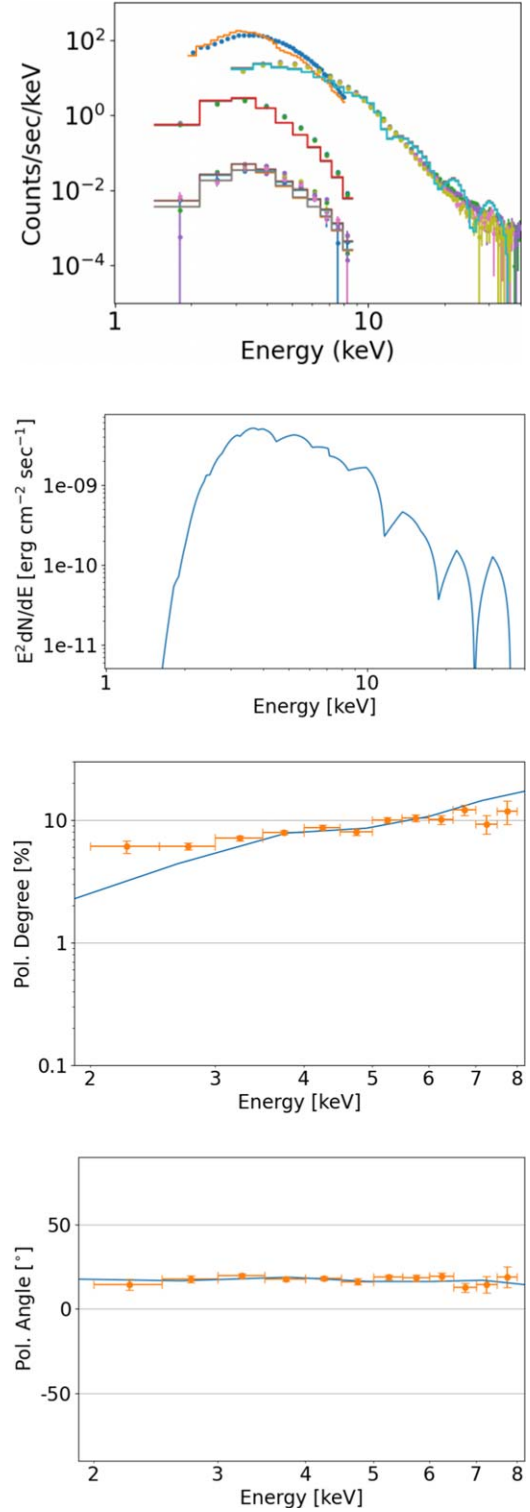

Figure 2. Same as Figure 1 but for extreme parameters that can reproduce the IXPE results (see Table 1 for the fit parameters). For the model, the black hole spin axis is at a PA of $-11°.83$. Note that the model assumes a thin accretion disk without any corona; the `kerrClight` optical depth parameter τ_C is thus zero. The model has a very low disk temperature, and most photons do not make it to high energies, resulting in large statistical fluctuations of the `kerrClight` predictions above a few keV.

through bremsstrahlung ($n_e > 2.3 \times 10^{19}$ cm^{-3}), a kinetic luminosity exceeding >100 times the Eddington luminosity would be required. We can thus exclude this scenario.

Assuming an outflowing scattering accretion disk atmosphere (or corona) gives rise to the strong polarization requires Thomson optical depths exceeding unity and thus a column density exceeding $1/\sigma_T \approx 1.5 \times 10^{24} \, \mathrm{cm}^{-2}$, with σ_T being the Thomson cross section. Using a black hole mass of $20 \, M_\odot$ and positing that the scattering plasma extends no more than $h_{\max} = 10 \, r_g$ above the accretion disk imply an electron density of $n_e > (h_{\max} \sigma_T)^{-1} \approx 5 \times 10^{16} \, \mathrm{cm}^{-3}$. The corresponding kinetic luminosity for an ion-electron plasma is 24% of the Eddington luminosity. The scenario of an outflowing scattering medium is thus energetically challenging but not excluded.

4. Expected Impact of Electron and Ion Anisotropies on the Polarization Signal

Particle (electron and ion) anisotropies impact the polarization of the bremsstrahlung and scattered emission from a plasma. It is well known that bremsstrahlung and Compton scattering are intimately related processes. In the framework of the Weizsäcker–Williams formalism, the properties of bremsstrahlung emission (including the polarization properties) can be derived by treating bremsstrahlung processes as the scattering of the virtual photons accompanying the target particle off the impinging particle (C. F. V. Weizsäcker 1934; E. J. Williams 1935; C. Brau 2003). The interested reader can find discussions of the polarization of Bremsstrahlung emission in E. Haug & W. Nakel (2004) and the polarization of scattered emission in G. Rybicki & A. Lightman (2008). Hard X-ray solar flares may be strongly polarized owing to polarized bremsstrahlung emission (D. J. Stackhouse & E. P. Kontar 2018 and references therein).

Although particle anisotropies of order unity can emit X-rays polarized at levels of several ten percent (see the Monte Carlo radiation transport simulations in the Appendix), the effect will likely not play a noticeable role in the case of the X-ray emission from BHXRBs in the soft state. The magnitude of the anisotropies will depend on the relative timescales for generating and damping the anisotropies. The anisotropies are expected to develop together with pressure anisotropies in the sheared plasma of differentially rotating accretion disks. The rotation will lead to the amplification of the toroidal magnetic field. As particles conserve their adiabatic invariants, the pressure perpendicular to the magnetic field $P_\perp$ and parallel to the magnetic field $P_\parallel$ evolve separately as

$$\frac{d}{dt}\left(\frac{P_\perp}{\rho B}\right) = 0, \quad \frac{d}{dt}\left(\frac{P_\parallel B^2}{\rho^3}\right) = 0, \tag{3}$$

where ρ is the plasma density and B is the magnetic field (G. F. Chew et al. 1956). The shear motion increasing B without changing ρ will lead to $P_\perp > P_\parallel$. On the other hand, if B decreases, $P_\parallel > P_\perp$ develops instead. We expect that such anisotropies develop on the dynamical timescale of $\sim 2\pi r_g/c \approx 6 \times 10^{-4}$ s.

The anisotropies will be damped by several processes. First, collisions will tend to isotropize the particle distribution. The resulting fractional pressure anisotropy is approximately given by

$$\frac{P_\perp - P_\parallel}{P} \sim \frac{1}{\nu}\frac{1}{B}\frac{dB}{dt} \sim \frac{u}{v_{th}}\frac{\lambda}{L_u}, \tag{4}$$

where ν is the collision rate, λ is the collisional mean free path, v_{th} is the thermal velocity of plasma particles, u is the (shear) flow velocity, and L_u is the length scale over which the velocity

varies (S. V. Komarov et al. 2016). Other processes that can limit the anisotropy include kinetic instabilities caused by the pressure anisotropy itself: the fire hose instability can develop when $P_\parallel/P_\perp > (1-2/\beta_\parallel)^{-1}$, and a mirror instability can develop in the opposite regime $P_\perp/P_\parallel > 1 + 1/\beta_\perp$, where $\beta_\parallel = P_\parallel/(B^2/8\pi)$ and $\beta_\perp = P_\perp/(B^2/8\pi)$ (e.g., M. W. Kunz et al. 2014). These instabilities lead to microscopic fluctuations that can scatter particles, leading to collisional effects that limit the pressure anisotropy at the threshold values. Alternative or additional mechanisms that can produce electron or ion anisotropies include particle heating or acceleration in shocks or through magnetic reconnection.

We can use the lower limits of the electron and ion densities in the photosphere or the scattering atmosphere of the 4U 1630–47 from Section 3 to estimate the anisotropy degrees that we can expect. For a scattering atmosphere, we derive the following constraints. Assuming a neutral pure hydrogen plasma, we infer an electron-ion collision timescale of (e.g., M. Kunz 2023)

$$\tau_{ei} = \frac{3 \sqrt{m_e} (k_B T_e)^{3/2}}{4 \sqrt{2} \pi n_e \lambda_e e^4} < 7.5 \times 10^{-8} \, \mathrm{s}, \tag{5}$$

with m_e the electron mass, $k_B T_e = 3.7 \, \mathrm{keV} \approx 5.9 \times 10^{-12}$ erg, the electron Coulomb logarithm $\lambda_e \approx 20$, and e the electron charge. The collisional timescale for ions is

$$\tau_{ii} = \frac{3 \sqrt{m_i} (k_B T_i)^{3/2}}{4 \sqrt{\pi} n_i \lambda_i e^4} < 4.6 \times 10^{-6} \, \mathrm{s}, \tag{6}$$

with the ion Coulomb logarithm $\lambda_i \approx 20$. These times are much shorter than the dynamical timescale of 6×10^{-4} s. If the anisotropies are generated on dynamical timescales, we thus expect the electron and ion anisotropies in a scattering atmosphere to be of the order of 10^{-4} and 10^{-2}, respectively. The electron and ion anisotropies in the photosphere are even smaller. For electron density n_e and ion density n_i the electron-ion Bremsstrahlung volume emissivity is (G. Rybicki & A. Lightman 2008)

$$\epsilon_{ff} \approx 1.7 \times 10^{-27} \sqrt{T} n_e n_i \, \mathrm{erg \, s^{-1} \, cm^{-3}}. \tag{7}$$

Assuming that the emission comes from a cylinder of inner and outer radii $2 \, r_g$ and $10 \, r_g$ and height $h_{\max} = 10 \, r_g$ as well as $n_e = n_i$, we infer electron and ion densities exceeding $2.3 \times 10^{19} \, \mathrm{cm}^{-3}$ so that the emitted power per area $\epsilon_{ff} h_{\max}$ equals the diluted blackbody emissivity $I = \sigma_B (T/f)^4 \approx 1.8 \times 10^{23} \, \mathrm{erg \, s^{-1} \, cm^{-2}}$ for $k_B T = 1.1 \, \mathrm{keV}$ and a hardening factor of $f = 1.7$. For these electron and ion densities, the electron-ion and ion-ion collisional timescales are 1.6×10^{-10} s and 10^{-8} s, respectively.

In summary, the intensity of the 4U 1630−47 HSS emission from the region close to the $\sim 20 \, M_\odot$ black hole precludes the generation of particle anisotropies of order unity that would be required to explain the strongly polarized signal from the source.

5. Summary and Discussion

In this Letter, we discuss the impact of several mechanisms on the polarization of the X-rays from 4U 1630−47. We show that a standard thin disk with or without corona can fit the flux and polarization energy spectra only when adopting distances <1 kpc, much smaller than the lower limits on the distance of

4U 1630−47 from E. Kalemci et al. (2018). Assuming a black hole mass of 40 $M_\odot$ and a distance of 0.35 kpc, we find a model with a high black hole spin of $a = 0.992$ that can generate high PDs owing to the dominance of reflected gravitationally lensed emission in the IXPE energy band.

Our calculations show that alternative explanations of the high polarization degrees involving relativistically moving electron-ion plasmas require high mechanical luminosities. The constraints are much weaker for a scattering electron-positron plasma. However, we are not aware of a mechanism to generate and accelerate a suitable electron-positron plasma close to the black hole that could intercept and scatter a large fraction of the thermally emitted X-rays.

We demonstrate that although anisotropic particles can emit strongly polarized bremsstrahlung and Comptonized emission, the plasma in the inner portions of BHXRBs in the soft state is likely to be too dense for noticeable particle anisotropies to develop.

A promising avenue for future work are slim disk models with other geometries than those explored by A. T. West & H. Krawczynski (2023). Fitting the data may require additional shadowing or reflecting features. As mentioned in the Section 1, scattering tends to produce energy-independent PDs. The apparent PD increase at higher energies could be the result of dust scattering reducing the net PDs at <5 keV energies. Such scenarios can possibly be tested by confronting detailed models of candidate geometries with the spectroscopic and polarimetric data.

Appendix
Impact of Particle Anisotropies on the X-Ray Polarization Signal

A.1. Monte Carlo Radiation Transport Simulations

This appendix discusses the polarization degrees and directions of the emission from plasmas with anisotropic particles. The study uses Monte Carlo radiation transport simulations similar to those of T. Bai & R. Ramaty (1978) and N. L. S. Jeffrey & E. P. Kontar (2011). They account for electron anisotropies but neglect ion anisotropies as well as polarized free–free self-absorption. Ion anisotropies would amplify the effect of electron anisotropies. Self-absorption always depolarizes a signal with the emission approaching an unpolarized signal in the limit of an optically thick plasma. We first describe the Monte Carlo code and subsequently present the results.

A.2. Monte Carlo Radiation Transport Simulations

We study two configurations making use of the scattering engine described in B. Beheshtipour et al. (2017). The first configuration is used to study the polarization of X-rays emitted by pure scattering atmospheres with anisotropic electrons. The photons are emitted at the bottom of the atmosphere extending from $z = -5\, l_{sc}$ to $z = 0$, with l_{sc} being the scattering mean-free path. We set the polarization of the emitted photons to 0 to clearly see the effect of the scatterings on the photon polarization.

Photons scatter off electrons drawn from a Maxwell–Boltzmann distribution of temperature T. The code uses four wavevectors $k^\mu = (E, E\boldsymbol{n})$ to keep track of the energy E and the direction $\boldsymbol{n}$ of a photon. The code keeps track of the photon's linear polarization with the help of two parameters: the PD of the photon and a polarization vector $f^\mu = (0, \boldsymbol{f})$ with $|\boldsymbol{f}| = 1$ encoding the electric field polarization direction (C. W. Misner et al. 2018). The Compton scattering is effected by Lorentz transforming k^μ and f^μ into the scattering electron's rest frame. After drawing a random direction of the scattered photon, we construct the Stokes vector of the incoming photon referenced to the plane spanned by the wavevectors of the incoming and outgoing photons. The Stokes vector of the outgoing photon is calculated by multiplying the Stokes vector of the incoming photon with Fano's fully relativistic scattering matrix (U. Fano 1957; W. H. McMaster 1961; B. Beheshtipour et al. 2017). A rejection algorithm uses the Stokes-I parameter of the scattered photon to account for the energy and scattering angle dependence of the Klein–Nishina cross section. The scattering changes the photon energy in the electron rest frame according to Compton's equation. The Stokes vector is subsequently used to infer the PD and polarization direction $\boldsymbol{f}$ of the scattered photon. In the last step, the wave and polarization vectors are transformed back into the plasma frame. We verified the code's performance by reproducing Chandrasekhar's results for a test run, in which we switched off all relativistic effects (change of electron energy, Klein–Nishima cross section, and scattering probability as a function of the angle between electron velocity and photon wavevector; see B. Beheshtipour et al. 2017). The Comptonization code was furthermore cross-checked in the deep Klein–Nishima regime against the MONK code (W. Zhang 2022, private communication).

The second configuration is used to study the impact of the polarized bremsstrahlung emission, photon absorption, and Compton scattering on the polarization of the emergent emission. We simulate a five-absorption-length-deep atmosphere at (electron) temperature T. The relative importance of emission and scattering is parameterized by the ratio $r_{sc/a}$ of the absorption to scattering cross sections, and we use the parameters n and m to characterize the electron anisotropy. Bremsstrahlung photons are emitted uniformly throughout the

atmosphere. The PD and PA are generated by making use of the relativistic cross sections σ_{II} and σ_{III} for the emission of photons polarized parallel and perpendicular to the plane defined by the electron and photon velocity vectors derived by R. L. Gluckstern & M. H. Hull (1953) in the first Born approximation. Note that Equations (4.2) and (4.3) of R. L. Gluckstern & M. H. Hull (1953) are correct up to a typo (multiplication instead of subtraction at the beginning of the last line of Equation (4.3)) that Gluckstern acknowledged in a private communication mentioned in T. Bai & R. Ramaty (1978). The reproductions of these equations by T. Bai & R. Ramaty (1978) include errors as do those of S. V. Komarov et al. (2016). The latter authors give the bremsstrahlung cross sections in a convenient form, but their Equation (16) for L includes a factor of 2 that should be dropped. In our code, photons propagate until they are absorbed, scatter, or escape the atmosphere. The Compton scatterings are simulated as explained above.

Photons escaping the atmosphere are sorted into six bins in the cosine of the inclination of the observer μ_{obs} and in five bins in energy, and the Stokes parameters within each bin are summed. Owing to the symmetry of the plane-parallel atmosphere, Stokes U vanishes. We denote electric field polarizations perpendicular to the atmosphere as positive polarization (PD $= Q/I > 0$) and polarizations parallel to the atmosphere as negative polarization (PD $= Q/I < 0$).

A.3. Results: Polarization of Scattered Emission

In the first step, we use the code to demonstrate how much electron anisotropies modify the PDs compared to the classical results for a pure electron scattering atmosphere derived by Chandrasekhar (S. Chandrasekhar 1960). Fitting the energy spectrum of 4U 1630–47 during the IXPE HSS observations with the diluted multitemperature blackbody model `ezdisk` (E. R. Zimmerman et al. 2005) gives a maximum blackbody temperature T_{BB} of 1.4 keV (A. Ratheesh et al. 2024). Using the temperature profile from the `ezdisk` model, this gives an emission-weighted blackbody temperature of 1.1 keV when averaging from $2\,r_{\mathrm{g}}$ to $10\,r_{\mathrm{g}}$. In the following, we assume a plasma with electron and ion temperatures T_{e} and T_{i} of 3.7 keV, as bremsstrahlung of a plasma at these temperatures generates an energy spectrum with a νF_ν high-energy cutoff similar to the one of a 1.1 keV blackbody. The simulations focus on a small local region of the accretion disk (or corona) modeled as a plane-parallel slab lying in the $x - y$-plane with the surface normal pointing along the z-direction. For a BHXRB, the z-axis would be parallel to the angular momentum vector of the inner accretion disk and presumably also parallel to the black hole angular momentum vector. The global effects from transporting the emission through the curved spacetime of a Kerr black hole and from reflecting the emission off the accretion disk are not considered here. Adding up the emission from different regions of the accretion disk will lower the net polarization degree.

We consider first the case in which the electrons move preferentially up and down in the emitting slab with a probability distribution:

$$p(\mu) \propto (\mu^2)^n, \qquad (A1)$$

with $n > 0$ and μ being the angle between the electron velocity and the z-axis. We parameterize the opposite behavior, electrons moving preferentially in the $x - y$-plane of the
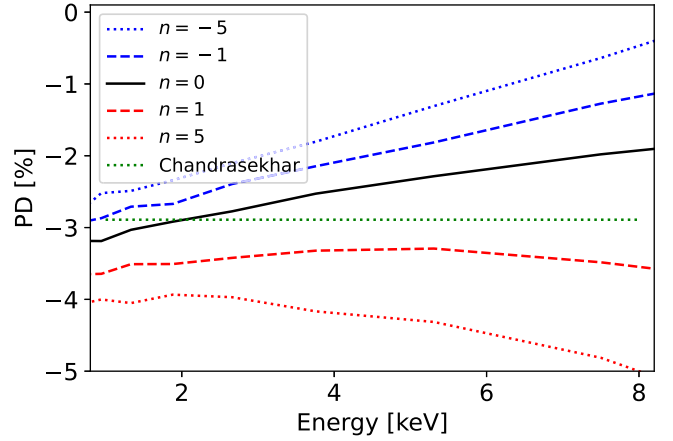

Figure 3. PDs produced by a pure electron scattering atmosphere at temperature $k_{\mathrm{B}}T = 3.7$ keV for an observer at inclination $i = 65°$. Positive PDs show a polarization perpendicular to the emitting plasma slab, and negative PDs show a polarization parallel to the emitting plasma slab. The lines show the results for $n = -5$ (blue dotted line), $n = -1$ (blue dashed line), $n = 0$ (black solid line), $n = 1$ (red dashed line), and $n = 5$ (red dotted line). The green dotted line shows Chandrasekhar's result for reference.

emitting slab, as

$$p(\mu) \propto (1 - \mu^2)^{|n|} \qquad (A2)$$

for $n < 0$. Throughout this Letter, we adopt the convention that positive (negative) PDs represent electric vector polarization directions perpendicular (parallel) to the emitting plasma slabs. Figure 3 shows the results for the likely 65° inclination of 4U 1630–47. Preferred electron motion perpendicular (parallel) to the slab with $n > 0$ ($n < 0$) increases (decreases) the polarization parallel to the slab.

Interestingly, the polarization degrees depend on energy owing to the correlation of the photon energy and the mean number of scatterings. We conclude that pronounced anisotropies can impact the PDs significantly.

A.4. Results: Polarization of Bremsstrahlung Emission

As mentioned above, the bremsstrahlung emission from anisotropic particles is polarized. For photon energies less than $\sim 1/10$ of the electron energy, the bremsstrahlung is polarized perpendicular to the electron direction as a consequence of small-angle electron scatterings. Conversely, for photon energies exceeding $\sim 1/10$ of the electron energy, the bremsstrahlung is polarized parallel to the electron direction as a consequence of large-angle electron scatterings. The polarization degree reaches 100% for photons with energies close to the energy of the emitting electron. As mentioned above, we assume a plasma temperature of 3.7 keV. Figure 4 shows the polarization energy spectra for the same electron anisotropies as above, for various ratios $r_{\mathrm{s/a}}$ of gray scattering-to-absorption cross sections. For $n = +1$ (electrons preferentially moving up and down), the scenario gives polarizations perpendicular to the surface normal with the 8 keV polarization degrees reaching $\sim 30\%$ for the most optimistic scenario that we simulated. For $n = -1$, the polarization direction is parallel to the disk and reaches $\sim 15\%$ at 8 keV for the most optimistic simulated scenario.

The shearing motion of the differentially rotating accretion flow is expected to produce a toroidal magnetic field in the accretion flow. For adiabatic changes of the magnetic field, the
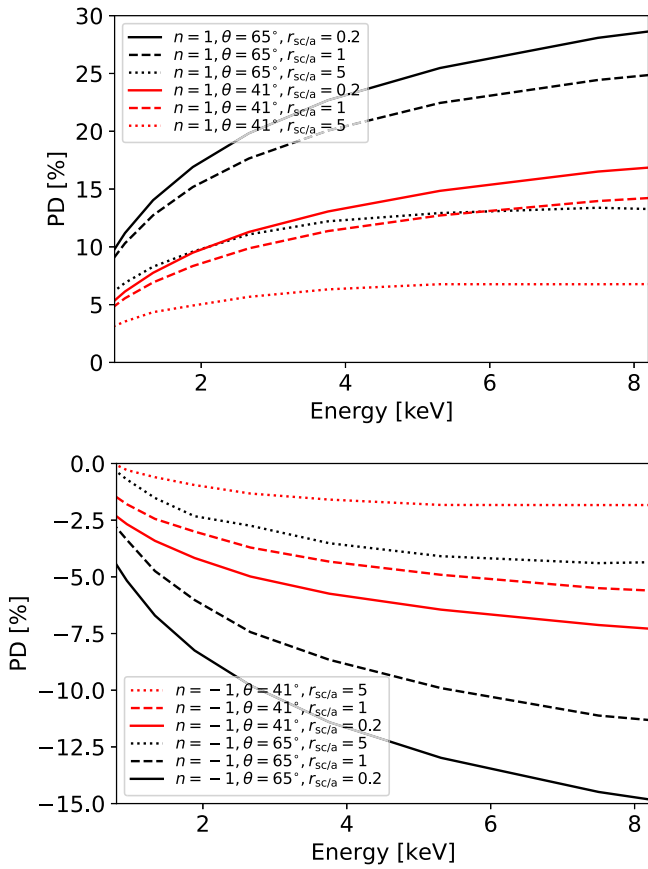
Figure 4. PDs produced by electrons moving preferentially perpendicular to the atmosphere ($n = 1$, upper panel) and parallel to the atmosphere ($n = -1$, lower panel) for observers at $i = 65°$ (black lines) and $i = 41°$ (red lines). For each color, the different lines show the results for different scattering-to-absorption cross section ratios: $r_{\mathrm{sc/a}} = 0.2$ (solid lines), 1 (dashed lines), and 5 (dotted lines).
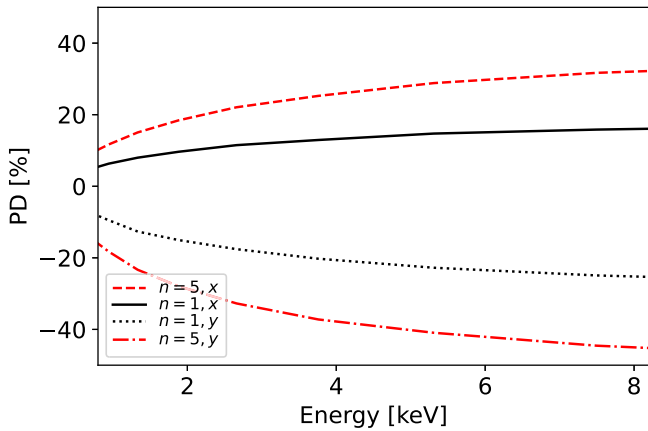

Figure 5. Polarization from electron with direction symmetric around the x-axis for $n = +1$ (black lines) and $n = +5$ (red lines) as seen for an $i = 65°$ observer viewing the atmosphere along the direction of the symmetry x-axis (dashed and solid lines) and perpendicular to it in the plane of the atmosphere (y-axis, dotted and dashed–dotted lines) for $r_{\mathrm{sc/a}} = 1$.

electrons gyrating around the field lines can develop anisotropies regarding the pitch angle of the electrons relative to the magnetic field lines. We studied such a scenario with electrons described by Equation (A1) but with μ being the pitch-angle cosine relative to the x-axis, assumed to be parallel to the magnetic field direction. Figure 5 shows the PDs for this

scenario. The results are somewhat more complicated as the PDs and PAs depend on the position of the observer relative to the x-axis. The net polarization would result from the superposition of the polarization from different regions of the disk. Global simulations would be required to show which polarization wins, taking into account strong gravitational lensing and gravitational and Doppler frequency shifts.

ORCID iDs

Henric Krawczynski (ID) https://orcid.org/0000-0002-1084-6507
Yajie Yuan (ID) https://orcid.org/0000-0002-0108-4774
Alexander Y. Chen (ID) https://orcid.org/0000-0002-4738-1168
Kun Hu (ID) https://orcid.org/0000-0002-9705-7948
Nicole Rodriguez Cavero (ID) https://orcid.org/0000-0001-5256-0278
Sohee Chun (ID) https://orcid.org/0009-0002-2488-5272
Ephraim Gau (ID) https://orcid.org/0000-0002-5250-2710
James F. Steiner (ID) https://orcid.org/0000-0002-5872-6061
Michal Dovčiak (ID) https://orcid.org/0000-0003-0079-1239

References

Bai, T., & Ramaty, R. 1978, ApJ, 219, 705
Baldini, L., Bucciantini, N., Lalla, N. D., et al. 2022, SoftX, 19, 101194
Beheshtipour, B., Krawczynski, H., & Malzac, J. 2017, ApJ, 850, 14
Brau, C. 2003, Modern Problems in Classical Electrodynamics (Oxford: Oxford Univ. Press), https://books.google.com/books?id=mUrawAEACAAJ
Capitanio, F., Campana, R., De Cesare, G., & Ferrigno, C. 2015, MNRAS, 450, 3840
Chandrasekhar, S. 1960, Radiative Transfer (New York: Dover Publications)
Chew, G. F., Goldberger, M. L., & Low, F. E. 1956, RSPSA, 236, 112
Dovciak, M., Steiner, J. F., Krawczynski, H., & Svoboda, J. 2023, ATel, 16084, 1
Fano, U. 1957, RvMP, 29, 74
García, J., Dauser, T., Reynolds, C. S., et al. 2013, ApJ, 768, 146
García, J., & Kallman, T. R. 2010, ApJ, 718, 695
Gluckstern, R. L., & Hull, M. H. 1953, PhRv, 90, 1030
Haug, E., & Nakel, W. 2004, The Elementary Process of Bremsstrahlung, World Scientific lecture notes in physics (Singapore: World Scientific)
Ingram, A., Bollemeijer, N., Veledina, A., et al. 2024, ApJ, 968, 76
Jana, A., & Chang, H.-K. 2024, MNRAS, 527, 10837
Jeffrey, N. L. S., & Kontar, E. P. 2011, A&A, 536, A93
Kalemci, E., Maccarone, T. J., & Tomsick, J. A. 2018, ApJ, 859, 88
Komarov, S. V., Khabibullin, I. I., Churazov, E. M., & Schekochihin, A. A. 2016, MNRAS, 461, 2162
Krawczynski, H., & Beheshtipour, B. 2022, ApJ, 934, 4
Krawczynski, H., & Beheshtipour, B. 2024, Monte Carlo Radiation Transport Code For Polarized Bremsstrahlung Emission and Compton Scattering By Anisotropic Electrons, v1, Zenodo, doi:10.5281/ZENODO.13904193
Krawczynski, H., Muleri, F., Dovciak, M., et al. 2022, Sci, 378, 650
Kunz, M. 2023, AST521 Lecture Notes (Princeton, NJ: Princeton Univ. Press), https://www.astro.princeton.edu/~kunz/Site/AST521/AST521_lecture_notes_Kunz.pdf
Kunz, M. W., Schekochihin, A. A., & Stone, J. M. 2014, PhRvL, 112, 205003
Kuulkers, E., Wijnands, R., Belloni, T., et al. 1998, ApJ, 494, 753
Li, L.-X., Narayan, R., & McClintock, J. E. 2009, ApJ, 691, 847
Li, L.-X., Zimmerman, E. R., Narayan, R., & McClintock, J. E. 2005, ApJS, 157, 335
Marra, L., Brigitte, M., Rodriguez Cavero, N., et al. 2024, A&A, 684, A95
McMaster, W. H. 1961, RvMP, 33, 8
Misner, C. W., Thorne, K. S., Wheeler, J. A., & Kaiser, D. I. 2018, Gravitation (Princeton, NJ: Princeton Univ. Press)
Nasa High Energy Astrophysics Science Archive Research Center (Heasarc) 2014, HEAsoft: Unified Release of FTOOLS and XANADU, Astrophysics Source Code Library, ascl:1408.004
Podgorny, J., Marra, L., Muleri, F., et al. 2023, MNRAS, 526, 5964
Podgorný, J., Svoboda, J., Dovčiak, M., et al. 2024, A&A, 686, L12
Ratheesh, A., Dovčiak, M., Krawczynski, H., et al. 2024, ApJ, 964, 77
Rodriguez Cavero, N., Marra, L., Krawczynski, H., et al. 2023, ApJL, 958, L8
Rodriguez Cavero, N. & IXPE Collaboration 2024, in Multifrequency Behavior of High Energy Cosmic Sources XIV (Trieste: SISSA), 39

Rybicki, G., & Lightman, A. 2008, Radiative Processes in Astrophysics, Physics textbook (New York: Wiley)

Schnittman, J. D., & Krolik, J. H. 2009, ApJ, 701, 1175

Shakura, N. I., & Sunyaev, R. A. 1973, A&A, 24, 337

Stackhouse, D. J., & Kontar, E. P. 2018, A&A, 612, A64

Steiner, J. F., Nathan, E., Hu, K., et al. 2024, ApJL, 969, L30

Svoboda, J., Dovčiak, M., Steiner, J. F., et al. 2024, ApJ, 960, 3

Taverna, R., Zhang, W., Dovciak, M., et al. 2020, MNRAS, 493, 4960

Tomaru, R., Done, C., & Odaka, H. 2024, MNRAS, 527, 7047

Tomsick, J. A., Lapshov, I., & Kaaret, P. 1998, ApJ, 494, 747

Veledina, A., Muleri, F., Dovčiak, M., et al. 2023, ApJL, 958, L16

Veledina, A., Muleri, F., Poutanen, J., et al. 2024, NatAs, 8, 1031

Veledina, A., Poutanen, J., Bocharova, A., et al. 2024, A&A, 688, L27

Weisskopf, M. C., Soffitta, P., Baldini, L., et al. 2022, JATIS, 8, 026002

Weizsäcker, C. F. V. 1934, ZPhy, 88, 612

West, A. T., & Krawczynski, H. 2023, ApJ, 957, 9

Williams, E. J. 1935, Kong. Dan. Vid. Sel. Mat. Fys. Med., 13N4, 1

Zhang, W., Dovčiak, M., & Bursa, M. 2019, ApJ, 875, 148

Zimmerman, E. R., Narayan, R., McClintock, J. E., & Miller, J. M. 2005, ApJ, 618, 832